

Chapman University Chapman University Digital Commons

Biology, Chemistry, and Environmental Sciences
Faculty Articles and Research

Science and Technology Faculty Articles and
Research

9-1-2016

Peroxiredoxin Catalysis at Atomic Resolution

Arden Perkins
Oregon State University

Derek Parsonage
Wake Forest University


Kimberly J. Nelson
Wake Forest University

O. Maduka Ogba
Chapman University, ogba@chapman.edu

Paul Ha-Yeon Cheong
Oregon State University

See next page for additional authors

Follow this and additional works at: https://digitalcommons.chapman.edu/sees_articles

 Part of the [Biological Phenomena, Cell Phenomena, and Immunity Commons](#), [Cell Anatomy Commons](#), [Cell Biology Commons](#), [Chemical and Pharmacologic Phenomena Commons](#), [Medical Biochemistry Commons](#), [Medical Cell Biology Commons](#), [Medicinal-Pharmaceutical Chemistry Commons](#), and the [Other Chemistry Commons](#)

Recommended Citation

Perkins A, Parsonage D, Nelson KJ, Ogba OM, Cheong PHY, Poole, LB, Karplus PA. Peroxiredoxin catalysis at atomic resolution. *Structure*. 2016;24(10):1668-1678. doi: 10.1016/j.str.2016.07.012

This Article is brought to you for free and open access by the Science and Technology Faculty Articles and Research at Chapman University Digital Commons. It has been accepted for inclusion in Biology, Chemistry, and Environmental Sciences Faculty Articles and Research by an authorized administrator of Chapman University Digital Commons. For more information, please contact laughtin@chapman.edu.

Peroxiredoxin Catalysis at Atomic Resolution

Comments

NOTICE: this is the author's version of a work that was accepted for publication in *Structure*. Changes resulting from the publishing process, such as peer review, editing, corrections, structural formatting, and other quality control mechanisms may not be reflected in this document. Changes may have been made to this work since it was submitted for publication. A definitive version was subsequently published in *Structure*, volume 24, issue 10, in 2016. It is freely available through Elsevier's open archive at DOI: [10.1016/j.str.2016.07.012](https://doi.org/10.1016/j.str.2016.07.012)

The Creative Commons license below applies only to this version of the article.

Creative Commons License



This work is licensed under a [Creative Commons Attribution-Noncommercial-No Derivative Works 4.0 License](https://creativecommons.org/licenses/by-nc-nd/4.0/).

Copyright

Elsevier

Authors

Arden Perkins, Derek Parsonage, Kimberly J. Nelson, O. Maduka Ogba, Paul Ha-Yeon Cheong, Leslie B. Poole, and P. Andrew Karplus



Published in final edited form as:

Structure. 2016 October 04; 24(10): 1668–1678. doi:10.1016/j.str.2016.07.012.

Peroxiredoxin Catalysis at Atomic Resolution

Arden Perkins^a, Derek Parsonage^b, Kimberly J. Nelson^b, O. Maduka Ogba^c, Paul Ha-Yeon Cheong^c, Leslie B. Poole^b, and P. Andrew Karplus^{a,*}

^aDepartment of Biochemistry and Biophysics, Oregon State University, Corvallis, OR 97331

^bDepartment of Biochemistry, Wake Forest School of Medicine, Winston-Salem, NC 27157

^cDepartment of Chemistry, Oregon State University, Corvallis, OR 97331

SUMMARY

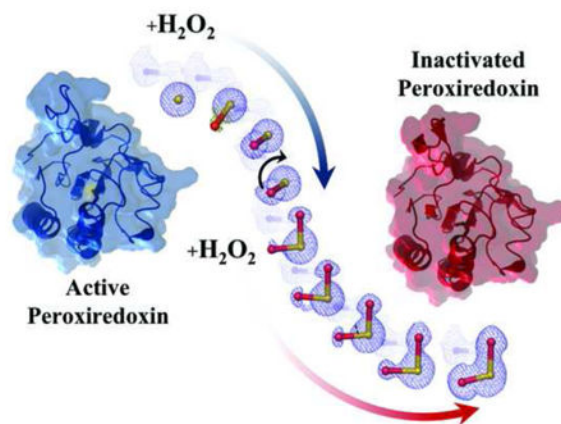
Peroxiredoxins (Prxs) are ubiquitous cysteine-based peroxidases that guard cells against oxidative damage, are virulence factors for pathogens, and are involved in eukaryotic redox regulatory pathways. We have analyzed catalytically active crystals to capture atomic resolution snapshots of a PrxQ-subfamily enzyme (from *Xanthomonas campestris*) proceeding through thiolate, sulfenate, and sulfinate species. These analyses provide structures of unprecedented accuracy for seeding theoretical studies, and show novel conformational intermediates giving insight into the reaction pathway. Based on a highly non-standard geometry seen for the sulfenate intermediate, we infer that the sulfenate formation itself can strongly promote local unfolding of the active site to enhance productive catalysis. Further, these structures reveal that preventing local unfolding, in this case via crystal contacts, results in facile hyperoxidative inactivation even for Prxs normally resistant to such inactivation. This supports previous proposals that conformation-specific inhibitors may be useful for achieving selective inhibition of Prxs that are drug targets.

Graphical Abstract

*To whom correspondence should be addressed: ph. 541-737-3200, fax: 541- 737-0481, karplusp@science.oregonstate.edu.

Author Contributions.

A.P. designed experiments, performed protein purification, crystallization, data analysis and interpretation, and wrote the text. D. P. performed cloning, protein purification, kinetic experiments, and reviewed the text. K. J. N. performed hyperoxidation experiments and reviewed the text. O. M. O. and P. H.-Y. C. performed all quantum mechanical computations and reviewed the text. L. B. P. and P. A. K. contributed to experimental design, data analysis, writing, and critical review of the text.



INTRODUCTION

Peroxiredoxins (Prxs) are ubiquitous peroxidases and in humans and other mammals they modulate peroxide signaling events that regulate biological phenomena such as cortisol production, cell senescence, and apoptosis (Hall et al., 2009)(Wood et al., 2003)(Perkins et al., 2014)(Rhee et al., 2012)(Kil et al., 2012). Prxs utilize a highly efficient cysteine-based mechanism to reduce hydrogen peroxide, organic hydroperoxides, and peroxyntirite at rates constants on the order of $10^3\text{--}10^7\text{ M}^{-1}\text{ s}^{-1}$ (Perkins et al., 2015). Though they perform catalysis in diverse ecological niches and redox environments, Prxs share a PxxxT/SxxC motif and conserved Arg (Nelson et al., 2010) that form a consistently organized active site (Fig. 1A, Fig. S1). The active site cysteine, referred to as the peroxidatic Cys (C_P), is stabilized as a reactive Cys-thiolate ($\text{C}_\text{P}\text{-S}^-$) by the active site environment and attacks a bound hydrogen peroxide to form Cys-sulfenate ($\text{C}_\text{P}\text{-SO}^-$) and water (Perkins et al., 2015) (Zeida et al., 2014)(Nagy et al., 2011)(Portillo-Ledesma et al., 2014). Most Prxs then undergo a substantial structural rearrangement to a locally unfolded (LU) conformation to allow C_P to form a disulfide with a second, often distant, resolving Cys (C_R). Subsequently, the $\text{C}_\text{P}\text{-C}_\text{R}$ disulfide is reduced, commonly by thioredoxin, to regenerate the reactive $\text{C}_\text{P}\text{-S}^-$ in the fully folded (FF) conformation (Perkins et al., 2015).

An additional complexity of Prx catalysis is a regulatory feature associated with further oxidation of C_P : if the FF active site is sufficiently stabilized and unfolding inhibited, a second peroxide can inactivate the enzyme by reacting with the FF $\text{C}_\text{P}\text{-SO}^-$ to “hyperoxidize” it to a Cys-sulfinate ($\text{C}_\text{P}\text{-SO}_2^-$) (Wood et al., 2003). So-called ‘sensitive’ Prxs of mammals and other eukaryotes that are readily hyperoxidized are thought to use this shunt for purposeful substrate-induced inactivation that enhances redox signaling possibly through allowing peroxide to persist and oxidatively regulate downstream targets (Wood et al., 2003). Such organisms also possess the enzyme sulfiredoxin (Srx) to resurrect hyperoxidized Prxs (Perkins et al., 2014). In contrast, ‘robust’ Prxs such as those from bacterial pathogens are thought to only be used for oxidative defense and have been evolutionarily optimized to resist hyperoxidation, even at millimolar concentrations of peroxides (Wood et al., 2003)(Lowther and Haynes, 2010).

Although previous studies have provided an excellent framework for understanding the Prx reaction pathway, important ambiguities remain regarding catalysis and hyperoxidation. Analysis of substrate-bound experimental structures (Hall et al., 2010) and computational studies (Zeida et al., 2014)(Nagy et al., 2011)(Portillo-Ledesma et al., 2014) have not yielded clarity about how the initial peroxidase step achieves a $\sim 10^2\text{--}10^6\text{ M}^{-1}\text{ s}^{-1}$ enhancement over free thiol (Nagy et al., 2011), with recent studies proposing differences in the key interactions occurring between C_P, the substrate, and the conserved Arg and Thr side chains (Fig. 1B–D)(Hall et al., 2010)(Zeida et al., 2014)(Portillo-Ledesma et al., 2014). Also poorly understood is the extent to which C_P-SO⁻ formation may promote local unfolding. Structural data for this state is limited to a few structures that do not show consistent interactions (Fig. S1), and due to the reactive nature of sulfenate/sulfenic acid, there can be uncertainty regarding the true redox state being observed (Perkins et al., 2013). The most thorough analysis to date comes from a study of four crystal structures (1.7 – 2.6 Å resolution) of the C_P-SO⁻ → C_P-SO₂⁻ transition in *Aeropyrum pernix* thiol peroxidase (ApTpx) that reported an unexpected C_P-sulfurane-His intermediate; but most Prxs do not contain this His residue, so such an intermediate cannot be present for the majority of Prxs (Nakamura et al., 2008).

To work towards resolving discrepancies in proposed peroxidation mechanisms and elucidate the relevant structural details important for unfolding and hyperoxidation, we sought a model system that could provide high resolution snapshots of Prx catalysis at all stages (e.g. C_P-S⁻; C_P-SO⁻; C_P-SO₂⁻; the C_P-C_R disulfide; and FF and LU conformations). We chose for this purpose *Xanthomonas campestris* peroxiredoxin Q (XcPrxQ). The PrxQ subgroup (formerly called BCP) is found in diverse organisms including bacteria, archaea, plants, and fungi, but not animals (Perkins et al., 2015)(Nelson et al., 2010), and some members of this subgroup have been shown to be important for pathogen defenses (Perkins et al., 2014). XcPrxQ was attractive for several reasons: (1) it possesses active site features common to the majority of Prxs; (2) as a monomeric Prx, it is more amenable to NMR and computational analyses; (3) it has yielded high resolution structures of an FF form (a C_P/C_R → Ser double mutant at 1.5 Å, PDB entry 3gkm), and an LU disulfide form (1.8 Å, PDB entry 3gkk) (Liao et al., 2009); and (4) the FF crystal form had an accessible active site, potentially enabling in-crystal studies of ligand binding and catalysis. XcPrxQ has its C_R residue in helix α₃, and undergoes a FF → LU conformation change involving the flipping of the C_P side chain and an unraveling of α₃ (Liao et al., 2009) (see Figure 3A).

Using this system, we have recently published the NMR backbone assignments for the reduced and oxidized states (Buchko et al., 2015) and here we report crystallographic studies that include analysis of wild-type crystals that are catalytically active and diffract better than anticipated. We have been able to capture at atomic resolution a full series of novel wild-type XcPrxQ structures that encompass the complete C_P-S⁻ → C_P-SO⁻ → C_P-SO₂⁻ transition and provide novel insights into Prx catalysis. The in-crystal behavior also demonstrates the extent to which even a robust bacterial Prx can be made highly sensitive to hyperoxidative inactivation.

RESULTS AND DISCUSSION

Recombinant wild type *XcPrxQ* as well as its $C_P \rightarrow \text{Ser}$ (C48S) and $C_R \rightarrow \text{Ser}$ (C84S) mutants were prepared in good yields and behaved well in analyses (see Experimental Procedures). In addition to basic functional characterization of the wild type enzyme we report 15 crystal structures refined at resolutions of 1.0 – 1.35 Å (Table 1, Table S1) that include a series of 12 novel structures of the catalytically active crystals of the FF wild type enzyme at various stages along the catalytic cycle, and one novel structure each of the C48S and C84S mutants, and the wild type enzyme disulfide form solved at ~0.5 Å higher than in a previous study (Liao et al., 2009).

Basic functional characterization of *XcPrxQ*

In a standard Prx assay system, recombinant *XcPrxQ* reduced hydrogen peroxide and organic peroxides with k_{cat}/K_m values of $\sim 3 \times 10^4 \text{ M}^{-1} \text{ s}^{-1}$ (Fig. 2A–B, Table S2). This level of activity is typical for PrxQ representatives, which range from 0.8×10^4 to $4 \times 10^4 \text{ M}^{-1} \text{ s}^{-1}$ (Reeves et al., 2011)(Rouhier et al., 2004)(Horta et al., 2010). The recombinant *XcPrxQ* was also relatively resistant to hyperoxidation in solution as is typical for bacterial Prxs (Fig. 2C–F) (Nelson et al., 2013). Quantifying the sensitivity using the $C_{\text{hyp}1\%}$ metric, which indicates the peroxide concentration at which 1% of the enzyme molecules will be oxidatively inactivated per turnover (Nelson et al., 2013), *XcPrxQ* has a value of 1.4 mM, and so is roughly 20-times more robust than human Prx I and 7 times less robust than *S. typhimurium* AhpC (Fig. 2F, Table S2).

High Precision Views of the FF and LU Active Sites

By pretreating the recombinant enzyme with dithiothreitol (DTT) we were able to grow FF crystals of the authentic reduced wild type form (Fig. 3A). These crystals diffracted to ~1.0 Å resolution, the best resolution so far for any Prx (Fig. S1). We were also able to replicate the crystals of the LU disulfide form (Fig. 3A) and extend their resolution to ~1.3 Å. For these structures, the high-quality electron density (Fig. 3B–C) clearly defines the active site geometry and allows us to precisely define, in the context of this model system, the active site interactions present in the substrate-ready FF active site (Fig. 1A–B) as well as those present in the disulfide form. In the unreacted protein, C_P (Cys48) interacts closely with the Arg123 side chain, the Lys42 backbone NH, and two water molecules that roughly mimic the oxygens of a peroxide substrate (Fig. 1A & 3B). The structure of C48S (i.e. $C_P \rightarrow \text{Ser}$) looks nearly the same but has a bound phosphate that displaces the waters to similarly mimic substrate binding (see Fig. 5C). Like other Prx crystal structures (Hall et al., 2010), the wild type structure has the Thr45 side chain positioned to donate a hydrogen bond to the Lys42 carbonyl oxygen and not to the Cys48- S_γ ($\text{O} \cdots \text{O}$ distance of 2.9 Å, Thr-CB- $\text{O}_\gamma \cdots \text{O}$ -Lys42 angle = 114°) (Fig. 1A & 3B). This consistent high precision positioning of Thr45 matches that seen in previous Prx structures (Hall et al., 2010), but contrasts with computational studies that have modeled the conserved Thr as donating a hydrogen bond to the Cys thiolate and/or substrate oxygen (Zeida et al., 2014)(Portillo-Ledesma et al., 2014) (Fig. 1B–D). We further observe that rather than bonding directly to the thiolate or ligand, the distal Arg NH is oriented at an intermediary position where it could stabilize the transition of the peroxide oxygen to the Cys S_γ (Fig. 1B–C, Fig. 3B).

Structures along the Reaction Path

Since the crystalline wild type protein, unlike the C_P→Ser mutant, is theoretically capable of catalysis if permitted by the crystal environment, we soaked the crystals with hydrogen peroxide, cumene hydroperoxide, and t-butyl hydroperoxide and found no loss in diffraction quality and conversion of C_P to the C_P-SO₂⁻ form (Fig. 4A,D and Fig. S2). After conducting initial experiments at pH 7.0, we performed additional substrate soaks varying peroxide concentrations and soak time, and also adjusted the pH to 4.5 speculating that a higher portion of protonated C_P (C_P-SH) could slow the reaction and allow us to better capture intermediates along the reaction pathway. This was successful and from a large set of structures solved, we selected a series of nine ~1 Å resolution structures – named FF₀ through FF₈ – that provide representative details of the transition of this Prx from C_P-S⁻ through C_P-SO⁻ to C_P-SO₂⁻ (Fig. 4; Tables 1 and S1); a tenth structure, FF₉, provides a fully-occupied C_P-SO₂⁻ reference structure at pH=7. The FF₀, FF₃, FF₅ and FF₈ structures (Table 1) provide the best views of the C_P-S⁻ (occupancy ~1), C_P-SO⁻ (occupancy ~0.5), ‘inverted’ C_P-SO⁻ (occupancy ~0.1), and C_P-SO₂⁻ (occupancy ~1) forms. The atomic resolution of these structures, with coordinate uncertainties of <0.05 Å, allow for a powerful dissection of the details of catalysis, including the reliable recognition of low occupancy intermediates and alternative conformations of active site residues.

Peroxidation (FF₁ through FF₃)—A known value of ultra-high resolution crystallography is its ability to provide definitive evidence for unexpected structures. Here, we were surprised that the clearly defined putative SO⁻ intermediate is stabilized in the crystal with a C_β-S_γ-O_δ bond angle of 153° (compared to the expected ~110 degrees (Engl and Huber, 1991)) and a short 1.38 Å S_γ-O_δ bond length (Fig. 5A,B). To our knowledge, such a bond angle has not been previously observed for a Cys-sulfenate. This is a reliable crystallographic result as we observed it in seven independent crystal structures: five H₂O₂ soaks at pH 4.5, one H₂O₂ soak at pH 7.0, and one t-butyl hydroperoxide soak at pH 7.0. The only standard hydrogen bond visible to the SO⁻ oxygen is from Arg123, but the moiety as a whole is fully surrounded by a tightly packed and well-ordered active site with low B-factors (Figs. 5A and 3A) that changes little between oxidation states. The presence of the sulfenate O_δ causes a conformation change of Pro41, which flexes from an exo to an endo rotamer to avoid a steric clash (Fig. 5B). Importantly, the change in Pro41 is also at half occupancy matching that of the SO⁻ oxygen. Interestingly, with this change the Pro41-C_δH atom is positioned to make a C-H hydrogen bond (Derewenda et al., 1995) to the SO⁻ oxygen (Fig. 5A). In a fortuitous related result, the structure of the C48S mutant contains a fully bound water in roughly the same position as the SO⁻ oxygen, and it similarly induces the Pro41 conformation change (Fig. 5C). This C48S structure provides evidence that despite the lack of multiple strong conventional hydrogen bonds, this is a thermodynamically favorable position for oxygen binding.

To better understand how this intermediate could adopt such an unexpected bond angle and length, we performed gas phase quantum mechanical (QM) computations of a variety of model methyl SOH and SO⁻ species (Figs. 5D, S4 and S5). These species incurred severe energetic penalties to adopt the observed geometry (~40–50 kcal/mol). Interestingly, a doubly protonated methyl SH₂O⁻ sulfenate species only exhibited ~9 kcal/mol of energetic

penalty for adopting the 153° angle (Fig. 5D). As we mentioned above, an Arg123-NH and a backbone amide (Lys42) provide universally conserved hydrogen bond interactions to the S_γ atom (Figs. 1A and 5A), and the geometry of these hydrogen bonding interactions are such that they may cause electronic effects that are similar to those caused by the double protonation. So while further studies are certainly needed to fully understand the nature of the structure seen, we hypothesize that the electrostatic (including hydrogen bonding) environment of the active site may help make this structure energetically accessible.

Hyperoxidation (FF₄ through FF₈)—Fortuitously, our model system allowed us to not only capture each chemical state of the catalytic cycle, but also aspects of the transition from C_P-SO⁻ to the hyperoxidized C_P-SO₂⁻ state (Fig. 4). In particular, structures FF₄ through FF₇ give evidence of a predicted (Hall et al., 2010) intermediate along this reaction pathway in which the SO⁻ rotates inward toward Arg123 to adopt what we call an ‘inverted’ position, and vacates the substrate binding site to permit reaction with a second peroxide. To accommodate the inverted sulfenate oxygen the side chain of Arg123 flips out of the active site and away from C_P (Fig 4C). Upon reaction with the second peroxide, Arg123 repositions to a third conformation to coordinate with the oxygens of the newly formed C_P-SO₂⁻ (Fig. 4D). Interestingly, we note for this bacterial Prx that both the inverted C_P-SO⁻ and C_P-SO₂⁻ reaction states along the hyperoxidation pathway perturb the Arg from its normal catalytic position.

Since XcPrxQ in solution is rather robust against hyperoxidation (Fig. 2F, Table S3), it was surprising that the protein in the crystal was so readily hyperoxidized and that the C_P-SO⁻ only accumulated to a maximal level of ~50%. In fact, for crystalline XcPrxQ the protein becomes fully hyperoxidized (with no disulfide formation) in a single turnover whereas only ~7 % would be expected to become hyperoxidized in solution at the same peroxide concentration (Fig. 2F). This can be easily understood in that crystal contacts block the protein from ever unfolding, effectively dropping the rate of disulfide bond formation to zero in the crystal compared with the solution rate of ~27 s⁻¹ (Table S2). In fact, crystal contact interactions occur at all four regions involved in local unfolding (Fig. 6A). While we cannot dissect how much each crystal contact contributes, we note that at one contact, Arg103 of a symmetry mate directly blocks disulfide formation by preventing rearrangement of the C_R-containing α3 helix (Fig. 6B).

Modulating the switch between local unfolding and hyperoxidation pathways

Susceptibility of Prxs to hyperoxidation and inactivation is of broad biological significance, as to survive pathogens must avoid having their Prxs inactivated by host-secreted reactive oxygen species, and inactivation is required as part of eukaryotic signaling pathways (Perkins et al., 2014). The structures reported here provide insight into the structural features involved in determining whether the protein in the C_P-SO⁻ state will undergo local unfolding or become hyperoxidized. For bacterial XcPrxQ, several lines of evidence indicate that sulfenate formation is destabilizing to the active site and promotes local unfolding. Initial formation of the sulfenate in XcPrxQ resulted in a high energy C_P-SO⁻ structure. As to why this sulfenate deviates so significantly from its ground state geometry, the main thing we notice is that the FF active site changes minimally between the thiolate (S⁻) and

sulfenate (SO^-) forms (Fig. 5C), and that within an unperturbed FF active site, the $\text{C}_\text{P}\text{-SO}^-$ sulfenate oxygen appears to be sterically and electrostatically hindered by the Thr45 side chain from adopting a relaxed position (Fig. 5A). We expect that in solution the unfavorable interactions would be relieved by local unfolding of the active site and facilitate formation of the $\text{C}_\text{P}\text{-C}_\text{R}$ disulfide, and we only observe this high energy conformation in the crystalline enzyme because of the stabilization of the FF active site conferred by the crystal contacts. Stated another way, for sulfenate formation there are two possibilities: the $\text{C}_\text{P}\text{-SO}^-$ adopts a relaxed geometry while perturbing the FF active site (i.e. promoting local unfolding) or the FF active site remains intact and the $\text{C}_\text{P}\text{-SO}^-$ adopts a high energy conformation compatible with its environment.

Interestingly, it has been observed that adopting a ground state sulfenate geometry perturbs the active site for Prxs from two other subfamilies. For human Prx6 (PDB entry 1prx)(Cao et al., 2011) the conserved Arg is swung away to make room for the modification, and for *Mycobacterium tuberculosis* AhpE (PDB entry 1xwv), a 1-Cys Prx, changes occur for both Arg and Thr positions (Li et al., 2005). Lastly, the tradeoff between sulfenate conformation and active site stability may explain the origin of the unusual hypervalent $\text{C}_\text{P}\text{-sulfurane-His}$ intermediate formed in peroxide soaks of crystals of the *A. pernix* thiol peroxidase (Nakamura et al., 2008); perhaps the intermediate is a high energy structure that forms in the crystal only because crystal contacts hinder the local unfolding that would normally be promoted by $\text{C}_\text{P}\text{-SO}^-$ formation.

A second structural determinant revealed in the *XcPrxQ* structures is how the transient inverted $\text{C}_\text{P}\text{-SO}^-$ affects the active site of a robust bacterial Prx. The rotation of the sulfenate oxygen to point back into the tightly packed active site causes the Arg to flip outward. Similar to the unfavorable geometry observed following initial peroxidation, these rearrangements would appear to promote local unfolding for the protein, and could also reduce the rate of hyperoxidation by removing the Arg's contributions to substrate binding and activation. Interestingly, we do not see the Arg to shift in response to an inverted oxygen position in sulfinate structures from sensitive Prx enzymes, such as human PrxII (PDB entry 1qmv)(Kitano et al., 2005), implying that sensitive Prxs could in part favor hyperoxidation over local unfolding by having evolved to better accommodate the inverted oxygen position in an FF active site.

Overall, the hyperoxidation pathway observed in the *XcPrxQ* structures reveal there are at least three ways the sensitivity of a Prx isoform can be tuned. First, hyperoxidation can be hindered if $\text{C}_\text{P}\text{-sulfenate}$ formation directly destabilizes the FF active site through unfavorable steric and electrostatic interactions, favoring local unfolding and promoting disulfide formation. Second, hyperoxidation can independently be further disfavored if the FF active site is destabilized when the sulfenate oxygen rotates to the inverted position and makes room for the second peroxide substrate to bind. Third, an enhancement of hyperoxidation can be accomplished through any set of interactions that disfavor local unfolding. In naturally sensitive Prx1 subfamily enzymes, a C-terminal extension buttresses and stabilizes the FF active site to inhibit unfolding and disulfide formation (Wood et al., 2003)(Perkins et al., 2014), and in the *XcPrxQ* crystals the functional equivalent of these interactions are the crystal contacts. An intriguing possibility is that this functionality could

be exploited to design conformation-trapping inhibitors to selectively target pathogen Prxs (Perkins et al., 2014) (Perkins et al., 2013). The advantage conferred by this strategy is that differences in FF \leftrightarrow LU conformational changes between human and pathogen isoforms could be leveraged to design inhibitors that bind regions other than the conserved active site, avoiding the potential for toxicity from disrupting human Prx function.

CONCLUSION

In summary, the ultra-high resolution structures reported here reveal in the context of bacterial *XcPrxQ* an unprecedented level of detail about active site interactions covering the full cycle of Prx catalysis (Fig. 6C). These structures directly add to our knowledge of the Prx mechanism, and will serve as ideal starting models for future computational studies of both the initial peroxidation reaction and hyperoxidative inactivation. An unusual Cys-sulfenate geometry is observed ($\angle C_{\beta}-S_{\gamma}-O_{\delta} = 153^{\circ}$) that quantum mechanical computations reveal incurs a severe energetic penalty that may be made more energetically accessible in the presence of strong hydrogen-bonds to the S_{γ} . From these results, we hypothesize that formation of the high energy sulfenate potentially induces the active site to locally unfold. Additionally, although several computational studies by others have modeled the conserved Thr as donating a hydrogen bond to the Cys thiolate and/or substrate oxygen (Zeida et al., 2014)(Portillo-Ledesma et al., 2014), consistent with previous structural studies of other Prxs (Hall et al., 2010) we find no evidence for such an interaction in the atomic resolution structures of *XcPrxQ*. Perhaps some of these discrepancies may be due to the exclusion of the universally conserved Pro and surrounding residues in earlier computational studies. Indeed, as with all model systems, the beneficial ease and simplicity of analysis conferred by aspects of *XcPrxQ* functionality come at the cost of limitations that some Prxs, a family that includes members separated by billions of years of evolution, may behave differently. Our structures here most directly represent the behavior of a robust bacterial Prx and further work will be required to explore how similar our observations are across the very diverse Prx family. However, we note that the *XcPrxQ* model system has the key Pro, Thr, Cys, and Arg residues conserved across all Prxs, and so we expect should be representative of the peroxidatic step, even though isoforms vary in the manner they locally unfold and in their susceptibility to hyperoxidation.

EXPERIMENTAL PROCEDURES

Materials & Methods

Cloning, Expression, and Purification—The gene for *XcPrxQ*, codon-optimized for expression in *E. coli* and synthesized by GenScript (Piscataway, NJ), was cloned between the *NcoI* and *HindIII* sites of pTHCm(Nelson et al., 2008) to express a non-His-tagged protein. Mutations were created using the QuikChange II method (Agilent). Expression was carried out in strain B834, using ZYM-5052 auto-induction medium at 37 °C (Studier, 2005). Purifications were done at 4 °C. Cells were disrupted using an Avestin C5 homogenizer, nucleic acids removed using streptomycin sulfate, and after overnight dialysis against 10 mM Tris-Cl, pH 8.0, 0.5 mM EDTA and centrifugation, the supernatant was loaded onto a 75 mL Q-Sepharose HP (GE Healthcare) column. *XcPrxQ* was eluted using a

0→1 M NaCl gradient, with *XcPrxQ*-containing fractions precipitated at 75 % saturating ammonium sulfate. The protein pellet was dissolved in a minimal volume of 25 mM potassium phosphate, pH 7.0, 1 mM EDTA and 0.1 M NaCl, and loaded onto a 250 mL Superose 12PG (GE Healthcare) column equilibrated with the same buffer. For assays, pure protein was buffer-exchanged into 20 mM Tris-Cl, pH 8.0, 1 mM EDTA, and concentrated to 10 mg ml⁻¹ by ultrafiltration, and frozen at -80 °C in aliquots. *E. coli* thioredoxin 1 (TrxA) and thioredoxin reductase (TrxR) were expressed and purified as previously described (Reeves et al., 2011).

Crystallography

Crystallization: After exchanging the wild type protein into 20 mM Tris pH 7.0, 20 mM sodium chloride, 1 mM EDTA, protein at 10 mg/ml was initially crystallized using conditions from Liao et al. (Liao et al., 2009). Crystal seeding greatly increased crystal size and growth rate. For wild type *XcPrxQ* in the locally unfolded disulfide form (LUss) optimal growth at 300 K occurred within three days in 4:1 protein:reservoir drops with a reservoir of 1.0 M ammonium sulfate, 0.2 M sodium chloride, 0.1 M sodium cacodylate, pH 6.8. From stacks of plate-like crystals, single plates were extracted into a 10 µL drop of AML containing a cryoprotectant of 4.5 M sodium formate, equilibrated for three minutes, then scooped and plunged into liquid nitrogen. Attempts at reducing the disulfide by chemical reductants were unsuccessful.

For initially crystallizing wild type *XcPrxQ* in the fully folded form (FF), the protein was pre-treated for 10 minutes with 10 mM DTT, and 10 mM fresh DTT was added to the condition previously reported to crystallize the C48S/C84S double mutant (Liao et al., 2009). After optimization, crystals were grown at 300 K in 6:2 µl protein:reservoir hanging drops with 8 mg/ml protein stock and a reservoir of 30% PEG 4000, 0.1 M sodium acetate pH 5.5, 10 mM DTT. Individual crystals were transferred to fresh 10 µL drops containing an AML of 18% PEG 4000, 0.1 M Tris, pH 7.0, and 4.5 M sodium formate, equilibrated for three minutes, scooped and plunged in liquid nitrogen.

For the wild type FF crystals, time courses at pH 7.0 were conducted with 10 mM t-butyl hydroperoxide or cumene hydroperoxide, and at pH 4.5 or 7.0 with 10 mM hydrogen peroxide, in a 10 µL drop. Substrate soaks were performed at 300 K by adding 1.0 µL of an 100 mM peroxide stock to a crystal-containing drop of 9 µL of AML with either 0.1 M sodium acetate (pH 4.5) or 0.1 M Tris (pH 7.0), and after between 5 s and 10 mins scooping and plunging the crystal into liquid nitrogen. A 10 mM substrate concentration was chosen as an amount that would not readily oxidize other residues non-specifically (Drozd et al., 1988) but was enough to readily oxidize C_p. That lower concentrations such a 1 mM did not consistently succeed can be explained by recognizing that for average crystals of ~1 × 0.5 × 0.2 mm³ (containing ca. 1.4 × 10¹⁵ *XcPrxQ* molecules), 1 mM peroxide in a 10 µL drop only provides roughly a 4:1 ratio of peroxide to protein. Due to the varying size and shapes of crystals, soak duration was only roughly correlated with the redox state observed in the structure. For this reason, we collected data on crystals with many different soak times to obtain structures for reaction intermediates.

The C48S and C84S single mutants crystallized in similar conditions to the wild type FF, in a protein buffer of 25 mM potassium phosphate, pH 7.0, 1 mM EDTA and 0.1 M NaCl. Optimal conditions for C48S were 3:1 μL protein:reservoir drops using a 6 mg/ml protein stock and a 40% PEG 4000, 0.1 M sodium acetate pH 5.5 reservoir. C84S crystallized in 4:1 μL protein:reservoir drops with 9.2 mg/ml protein stock and a reservoir of 35% PEG 4000, 0.1 M sodium acetate pH 5.5, 1 mM DTT. The C84S structure demonstrated no major differences other than a shift in the Ser position relative to the wild type Cys (Fig. S3), but we have included it here as it is the highest resolution structure for a C_R mutant form and may be useful for future studies. As for wild type, these crystals were generally equilibrated in a 10 μL drop of AML at pH 7.0 prior to freezing. The one exception was a C48S crystal harvested directly from its drop (at pH 5.5) that yielded the phosphate-bound structure. Crystals of wild type and C84S scooped directly from their drops did not yield phosphate-bound structures.

Data Collection: Data were collected at the Advanced Light Source at Lawrence Berkeley National Labs on beamlines 5.0.1, 5.02, and 5.03 at cryo-temperatures. Data were indexed and integrated with iMosflm 7.0.9 (Battye et al., 2011), and found to be in the two expected $P2_1$ crystal forms for LUs (wild type) and FF crystals (yielding wild type, C48S, and C84S structures) (Table 1, Table S1)(Liao et al., 2009). Though both crystal forms coincidentally have $P2_1$ symmetry, they have different unit cells and crystal packing interactions.

Refinement: For the FF structures, the main initial changes from entry 3gkm were the addition of ca. 100 water molecules now visible with the improved resolution and an alternate chain path for residues 65–67. Additionally, mass spectrometry implied the N-terminal methionine had been lost and an acetyl group gained, and this modification was reasonably clear in the electron density and was modeled. Several solvent sites exhibiting strong electron density and close bond distances of $\sim 2.1 \text{ \AA}$ were modeled as Na^+ ions, present in the protein buffer, crystallization conditions, and cryoprotectant. Continuous density near Cys84 may be a disordered PEG molecule, but was left unmodeled. Strong density for a tetragonal ligand was seen in the C48S active site at pH 5.5. This was modeled as a phosphate since the protein buffer contained 25 mM phosphate and because anomalous maps showed strong peaks for cysteine sulfur atoms but no signal at the ligand peak. In late stages of refinement, riding hydrogens were added, reducing R_{free} by $\sim 1 \%$. Subsequently, individual anisotropic B-factors were introduced for all non-hydrogen atoms, reducing R_{free} by a further 2–3 %.

For wild type structures treated with substrate, the occupancies of oxygen adducts were estimated from the relative strength of the electron density, with the expectation that B-factors would be slightly higher for the oxygen positions than the S_γ , the requirement that occupancies must add to 100%, the knowledge of the atom positions in the thiolate, sulfenate, and sulfinic acid forms based on clear high occupancy structures for each of those, and also using information from active site rearrangements that appear to be correlated with the redox changes at C_p . The final occupancies chosen also minimized residual difference peaks. We could not explicitly distinguish between sulfenate and sulfinic acid forms which differ by only a hydrogen (for example between alternate conformations of sulfenate and

low occupancy sulfinate). We tested if the extended sulfenate angle could be the result of radiation damage from data collection, but analysis of only the first 90 diffraction images still show the clearly-defined adduct.

Quantum mechanical computations—All quantum mechanical computations were performed in the gas phase using M06-2X(Zhao and Truhlar, 2008)/6-31G*(Miertuš et al., 1981) level of theory as implemented in Gaussian 09.(Frisch et al., 2009) Ten methyl sulfenate (SO^-) and sulfenic acid (SOH) species of varying oxidation and protonation states were computed for a series of geometries with varying C-S-O angles from 95° to 155° in 5° increments (Figs. S4, S5, & S5). For the methyl SOH species, the torsional angle around the S-O bond was rotated 360° in 10° increments for each C-S-O angle increment to capture the minimum energy pathway We benchmarked M06-2X/6-31G* results against energies from fifteen quantum mechanical methods including the high accuracy DLPNO-CCSD(T) (Fig. S5). The employed method yields consistent results at a lesser computational expense.

Measurement of Kinetic Properties—*XcPrxQ* activity was measured by following the decrease in fluorescence of *E. coli* thioredoxin, TrxA, as the reductant of *XcPrxQ* in reaction mixtures with H_2O_2 or cumene hydroperoxide, as described by Parsonage et al (2010) (Parsonage et al., 2010). Values for V_{\max} and K_m for both peroxide and TrxA substrates were calculated directly from global fits of all of the data for each peroxide substrate by using the multiple-function nonlinear regression capability of SigmaPlot (SYSTAT software) (Parsonage et al., 2010). The kinetic data using were fit to a model of saturable interactions (defined K_M) for each substrate, but the K_M for interaction of *EcTrxA* with *XcPrxQ* is not well determined given the concentrations used (Table S2). Steady state kinetic parameters from these global fits are reported in Table S2.

Hyperoxidation of *XcPrxQ* ($1 \mu\text{M}$) was measured in the presence of $1 \mu\text{M}$ *EcTrxA*, $0.1 \mu\text{M}$ *EcTrxR*, $150 \mu\text{M}$ NADPH, and either CHP or H_2O_2 (0.1, 0.2, 0.5, 1, 2, and 5 mM) in 25 mM potassium phosphate, pH 7.0, 1 mM EDTA, 100 mM ammonium sulfate at 25°C with a Varian Cary 50 UV-Vis spectrophotometer by monitoring absorbance at 340 nm. As the Prx protein becomes hyperoxidized over the course of the reaction (with a fraction inactivated during each turnover), the absorbance change over time increasingly deviates from linear kinetics. The kinetic trace was fit to an exponential decay model to describe inactivation sensitivity using the previously introduced $C_{\text{hyp}1\%}$ metric, which indicates the peroxide concentration at which 1% of the enzyme molecules will be oxidatively inactivated per turnover(Nelson et al., 2013). Steady state kinetic parameters from these global fits are reported in Table S2. Inactivation of *XcPrxQ* over 15 min during turnover with peroxide concentrations in excess of 0.1 mM was detectable and yielded a $C_{\text{hyp}1\%}$ value of 1.43 mM for H_2O_2 (Table S3).

Supplementary Material

Refer to Web version on PubMed Central for supplementary material.

Acknowledgments

This research was funded in part by National Institutes of Health grants GM050389 and GM119227 to LBP and PAK. PHYC is the Bert and Emelyn Christensen professor and acknowledges financial support from the Stone family of OSU. PHYC and OMO acknowledge computing infrastructure in part provided by the National Science Foundation Phase-2 CCI, Center for Sustainable Materials Chemistry (CHE-1102637). The Advanced Light Source is supported by the Director, Office of Science, Office of Basic Energy Sciences, of the U.S. Department of Energy under Contract No. DE-AC02-05CH11231.

Abbreviations

Prx	peroxiredoxin
TrxA	thioredoxin 1
Srx	sulfiredoxin
PDB	protein databank
C_P	peroxidatic cysteine
C_R	resolving cysteine
FF	fully folded
LU	locally unfolded
XcPrxQ	<i>Xanthomonas campestris</i> peroxiredoxin Q
ML	mother liquor
AML	artificial mother liquor
ρ_{rms}	root-mean-square electron density

References

- Afonine PV, Grosse-Kunstleve RW, Echols N, Headd JJ, Moriarty NW, Mustyakimov M, Terwilliger TC, Urzhumtsev A, Zwart PH, Adams PD. Towards automated crystallographic structure refinement with phenix refine. *Acta Crystallographica Section D Biological Crystallography*. 2012; 68:352–367. [PubMed: 22505256]
- Battye TGG, Kontogiannis L, Johnson O, Powell HR, Leslie AGW. iMOSFLM: a new graphical interface for diffraction-image processing with MOSFLM. *Acta Crystallographica Section D Biological Crystallography*. 2011; 67:271–281. [PubMed: 21460445]
- Buchko GW, Perkins A, Parsonage D, Poole LB, Karplus PA. Backbone chemical shift assignments for *Xanthomonas campestris* peroxiredoxin Q in the reduced and oxidized states: a dramatic change in backbone dynamics. *Biomol NMR Assign*. 2015:1–5.
- Cao Z, Tavender TJ, Roszak AW, Cogdell RJ, Bulleid NJ. Crystal structure of reduced and of oxidized peroxiredoxin IV enzyme reveals a stable oxidized decamer and a non-disulfide-bonded intermediate in the catalytic cycle. *J Biol Chem*. 2011; 286:42257–42266. [PubMed: 21994946]
- Davis IW, Murray LW, Richardson JS, Richardson DC. MOLPROBITY: structure validation and all-atom contact analysis for nucleic acids and their complexes. *Nucleic Acids Research*. 2004; 32:W615–W619. [PubMed: 15215462]
- Derewenda ZS, Lee L, Derewenda U. The Occurrence of C–H ··· O Hydrogen Bonds in Proteins. *Journal of Molecular Biology*. 1995; 252:248–262. [PubMed: 7674305]

- Driggers CM, Cooley RB, Sankaran B, Hirschberger LL, Stipanuk MH, Karplus PA. Cysteine Dioxygenase Structures from pH 4 to 9: Consistent Cys-Persulfenate Formation at Intermediate pH and a Cys-Bound Enzyme at Higher pH. *Journal of Molecular Biology*. 2013; 425:3121–3136. [PubMed: 23747973]
- Drozd R, Naskalski JW, Sznajd J. Oxidation of amino acids and peptides in reaction with myeloperoxidase, chloride and hydrogen peroxide. *Biochim Biophys Acta*. 1988; 957:47–52. [PubMed: 2846070]
- Emsley P, Cowtan K. Coot: model-building tools for molecular graphics. *Acta Crystallographica Section D Biological Crystallography*. 2004; 60:2126–2132. [PubMed: 15572765]
- Engh RA, Huber R. Accurate bond and angle parameters for X-ray protein structure refinement. *Acta Crystallographica Section A Foundations of Crystallography*. 1991; 47:392–400.
- Evans PR, Murshudov GN. How good are my data and what is the resolution? *Acta Crystallographica Section D Biological Crystallography*. 2013; 69:1204–1214. [PubMed: 23793146]
- Frisch, Mj; Trucks, GW.; Schlegel, HB.; Scuseria, GE.; Robb, MA.; Cheeseman, JR.; Scalmani, G.; Barone, V.; Mennucci, B.; Petersson, GA., et al. Gaussian 09, revision A. 02. Vol. 19. Gaussian, Inc; Wallingford, CT: 2009. p. 227-238.
- Hall A, Karplus PA, Poole LB. Typical 2-Cys peroxiredoxins – structures, mechanisms and functions. *FEBS Journal*. 2009; 276:2469–2477. [PubMed: 19476488]
- Hall A, Parsonage D, Poole LB, Karplus PA. Structural Evidence that Peroxiredoxin Catalytic Power Is Based on Transition-State Stabilization. *Journal of Molecular Biology*. 2010; 402:194–209. [PubMed: 20643143]
- Horta BB, Oliveira MAD, Discola KF, Cussioli JRR, Netto LES. Structural and Biochemical Characterization of Peroxiredoxin Q β from *Xylella Fastidiosa* CATALYTIC MECHANISM AND HIGH REACTIVITY. *J Biol Chem*. 2010; 285:16051–16065. [PubMed: 20335172]
- Karplus PA, Diederichs K. Linking Crystallographic Model and Data Quality. *Science*. 2012; 336:1030–1033. [PubMed: 22628654]
- Kil IS, Lee SK, Ryu KW, Woo HA, Hu MC, Bae SH, Rhee SG. Feedback Control of Adrenal Steroidogenesis via H₂O₂-Dependent, Reversible Inactivation of Peroxiredoxin III in Mitochondria. *Molecular Cell*. 2012; 46:584–594. [PubMed: 22681886]
- Kitano K, Kita A, Hakoshima T, Niimura Y, Miki K. Crystal structure of decameric peroxiredoxin (AhpC) from *Amphibacillus xylanus*. *Proteins*. 2005; 59:644–647. [PubMed: 15770647]
- Legault, CY. CYLview, version 1.0 b. Université de Sherbrooke; Sherbrooke, Quebec, Canada: 2009.
- Li S, Peterson NA, Kim MY, Kim CY, Hung LW, Yu M, Lakin T, Segelke BW, Lott JS, Baker EN. Crystal Structure of AhpE from *Mycobacterium tuberculosis*, a 1-Cys peroxiredoxin. *Journal of Molecular Biology*. 2005; 346:1035–1046. [PubMed: 15701515]
- Liao SJ, Yang CY, Chin KH, Wang AHJ, Chou SH. Insights into the Alkyl Peroxide Reduction Pathway of *Xanthomonas campestris* Bacterioferritin Comigratory Protein from the Trapped Intermediate–Ligand Complex Structures. *Journal of Molecular Biology*. 2009; 390:951–966. [PubMed: 19477183]
- Lowther WT, Haynes AC. Reduction of Cysteine Sulfinic Acid in Eukaryotic, Typical 2-Cys Peroxiredoxins by Sulfiredoxin. *Antioxidants & Redox Signaling*. 2010; 15:99–109. [PubMed: 20712415]
- Miertuš S, Scrocco E, Tomasi J. Electrostatic interaction of a solute with a continuum. A direct utilization of AB initio molecular potentials for the prevision of solvent effects. *Chemical Physics*. 1981; 55:117–129.
- Nagy P, Karton A, Betz A, Peskin AV, Pace P, O'Reilly RJ, Hampton MB, Radom L, Winterbourn CC. Model for the Exceptional Reactivity of Peroxiredoxins 2 and 3 with Hydrogen Peroxide A KINETIC AND COMPUTATIONAL STUDY. *J Biol Chem*. 2011; 286:18048–18055. [PubMed: 21385867]
- Nakamura T, Yamamoto T, Abe M, Matsumura H, Hagihara Y, Goto T, Yamaguchi T, Inoue T. Oxidation of archaeal peroxiredoxin involves a hypervalent sulfur intermediate. *PNAS*. 2008; 105:6238–6242. [PubMed: 18436649]
- Nelson KJ, Parsonage D, Hall A, Karplus PA, Poole LB. Cysteine pK_a Values for the Bacterial Peroxiredoxin AhpC \ddagger . *Biochemistry*. 2008; 47:12860–12868. [PubMed: 18986167]

- Nelson KJ, Knutson ST, Soito L, Klomsiri C, Poole LB, Fetrow JS. Analysis of the peroxiredoxin family: Using active-site structure and sequence information for global classification and residue analysis. *Proteins: Structure, Function, and Bioinformatics*. 2010; 79:947–964.
- Nelson KJ, Parsonage D, Karplus PA, Poole LB. Evaluating peroxiredoxin sensitivity toward inactivation by peroxide substrates. *Meth Enzymol*. 2013; 527:21–40. [PubMed: 23830624]
- Parsonage D, Desrosiers DC, Hazlett KRO, Sun Y, Nelson KJ, Cox DL, Radolf JD, Poole LB. Broad specificity AhpC-like peroxiredoxin and its thioredoxin reductant in the sparse antioxidant defense system of *Treponema pallidum*. *PNAS*. 2010; 107:6240–6245. [PubMed: 20304799]
- Perkins A, Gretes MC, Nelson KJ, Poole LB, Karplus PA. Mapping the Active Site Helix-to-Strand Conversion of CxxxxC Peroxiredoxin Q Enzymes. *Biochemistry*. 2012; 51:7638–7650. [PubMed: 22928725]
- Perkins A, Nelson KJ, Williams JR, Parsonage D, Poole LB, Karplus PA. The Sensitive Balance between the Fully Folded and Locally Unfolded Conformations of a Model Peroxiredoxin. *Biochemistry*. 2013; 52:8708–8721. [PubMed: 24175952]
- Perkins A, Poole LB, Karplus PA. Tuning of Peroxiredoxin Catalysis for Various Physiological Roles. *Biochemistry*. 2014; 53:7693–7705. [PubMed: 25403613]
- Perkins A, Nelson KJ, Parsonage D, Poole LB, Karplus PA. Peroxiredoxins: guardians against oxidative stress and modulators of peroxide signaling. *Trends Biochem Sci*. 2015; 40:435–445. [PubMed: 26067716]
- Portillo-Ledesma S, Sardi F, Manta B, Tourn MV, Clippe A, Knoops B, Alvarez B, Coitino EL, Ferrer-Sueta G. Deconstructing the catalytic efficiency of peroxiredoxin-5 peroxidatic cysteine. *Biochemistry*. 2014
- Reeves SA, Parsonage D, Nelson KJ, Poole LB. Kinetic and Thermodynamic Features Reveal That *Escherichia coli* BCP Is an Unusually Versatile Peroxiredoxin. *Biochemistry*. 2011; 50:8970–8981. [PubMed: 21910476]
- Rhee SG, Woo HA, Kil IS, Bae SH. Peroxiredoxin Functions as a Peroxidase and a Regulator and Sensor of Local Peroxides. *J Biol Chem*. 2012; 287:4403–4410. [PubMed: 22147704]
- Rouhier N, Gelhaye E, Gualberto JM, Jordy MN, Fay ED, Hirasawa M, Duplessis S, Lemaire SD, Frey P, Martin F, et al. Poplar Peroxiredoxin Q. A Thioredoxin-Linked Chloroplast Antioxidant Functional in Pathogen Defense. *Plant Physiol*. 2004; 134:1027–1038. [PubMed: 14976238]
- Sevilla F, Camejo D, Ortiz-Espín A, Calderón A, Lázaro JJ, Jiménez A. The thioredoxin/ peroxiredoxin/sulfiredoxin system: current overview on its redox function in plants and regulation by reactive oxygen and nitrogen species. *J Exp Bot*. 2015:erv146.
- Studier FW. Protein production by auto-induction in high-density shaking cultures. *Protein Expression and Purification*. 2005; 41:207–234. [PubMed: 15915565]
- Wood ZA, Poole LB, Karplus PA. Peroxiredoxin Evolution and the Regulation of Hydrogen Peroxide Signaling. *Science*. 2003; 300:650–653. [PubMed: 12714747]
- Zeida A, Reyes AM, Lebrero MCG, Radi R, Trujillo M, Estrin DA. The extraordinary catalytic ability of peroxiredoxins: a combined experimental and QM/MM study on the fast thiol oxidation step. *Chem Commun*. 2014; 50:10070–10073.
- Zhao Y, Truhlar DG. The M06 suite of density functionals for main group thermochemistry, thermochemical kinetics, noncovalent interactions, excited states, and transition elements: two new functionals and systematic testing of four M06-class functionals and 12 other functionals. *Theoretical Chemistry Accounts*. 2008; 120:215–241.

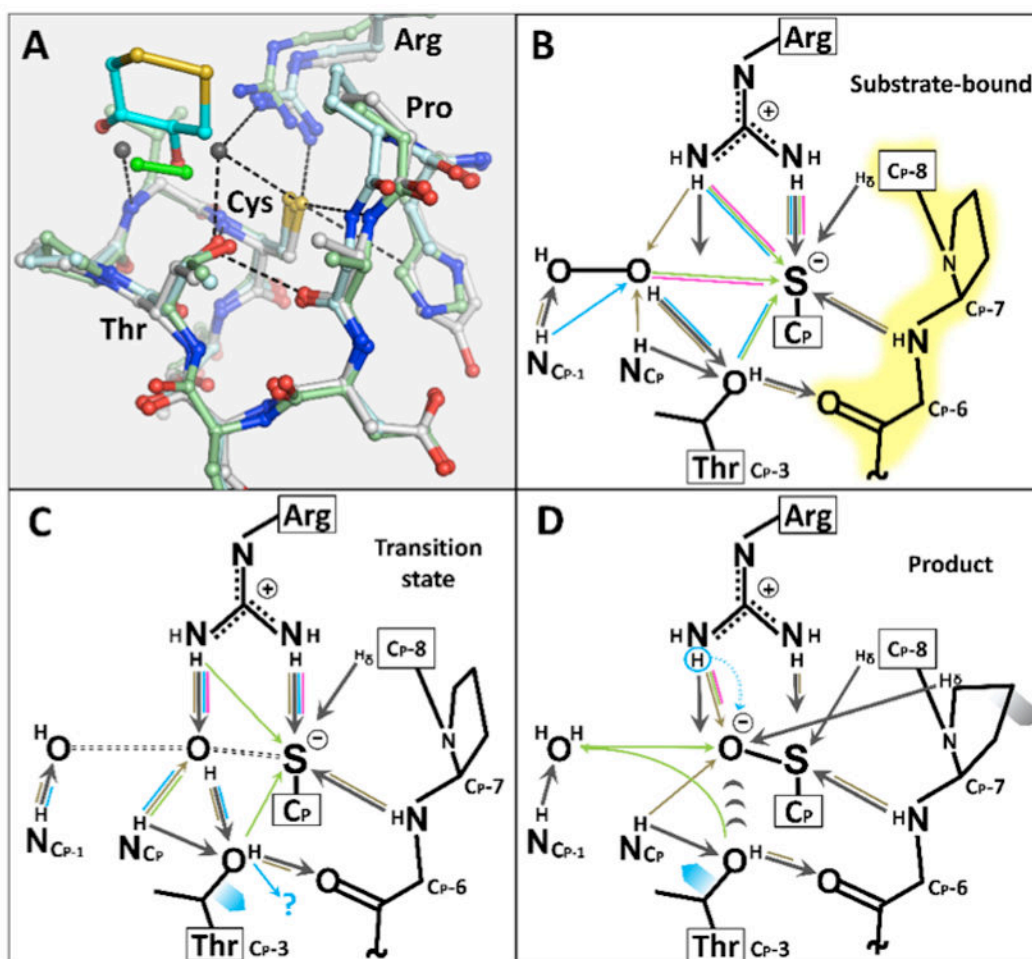


Figure 1.

Summary of proposed mechanisms of Prx peroxidation. **A.** Overlay of active sites of DTT-bound human PrxV (light blue) and peroxide-bound *ApTpx* (green) with water-bound wild-type *XcPrxQ* (white), with ligands colored cyan (DTT), lime (H_2O_2), and dark gray (waters), respectively. Dashed lines indicate active site interactions for *XcPrxQ*, including a contact between the C δ H of Tyr40 with the thiolate that would also contribute weak electrostatic stabilization to the thiolate. This appears to be a conserved interaction in FF Prx structures and involves either a Tyr or His. **B–D.** Previous studies do not provide a consensus on how Prx catalysis proceeds, as evident by the many different hydrogen bond interactions and residue shifts proposed. Hydrogen bonds seen in the *XcPrxQ* structures in this study (dark gray arrows pointing from donor to acceptor) for the substrate-bound state, the inferred transition state (based on relative rigidity of active site residues), and the product states, are compared with those proposed by previous studies: brown arrows for Hall et al. (Hall et al., 2010), blue arrows for Portillo et al. (Portillo-Ledesma et al., 2014), green arrows for Zeida et al. (Zeida et al., 2014), and pink arrows for Nagy et al. (Nagy et al., 2011). Shifts in residue positions are noted by thick arrows (Thr shift in blue panels C/D and Pro shift in dark gray in panel D). Forming and breaking covalent bonds are depicted as double dashed lines. Atoms not incorporated into previous QM simulations, presumably because they were

not thought to play key roles in the chemistry of catalysis, are highlighted in yellow in panel B. The circled hydrogen and dashed arrow in panel D notes a predicted proton transfer by Portillo et al. (Portillo-Ledesma et al., 2014). See also Fig. S1 for an analysis of available Prx crystal structures.

Author Manuscript

Author Manuscript

Author Manuscript

Author Manuscript

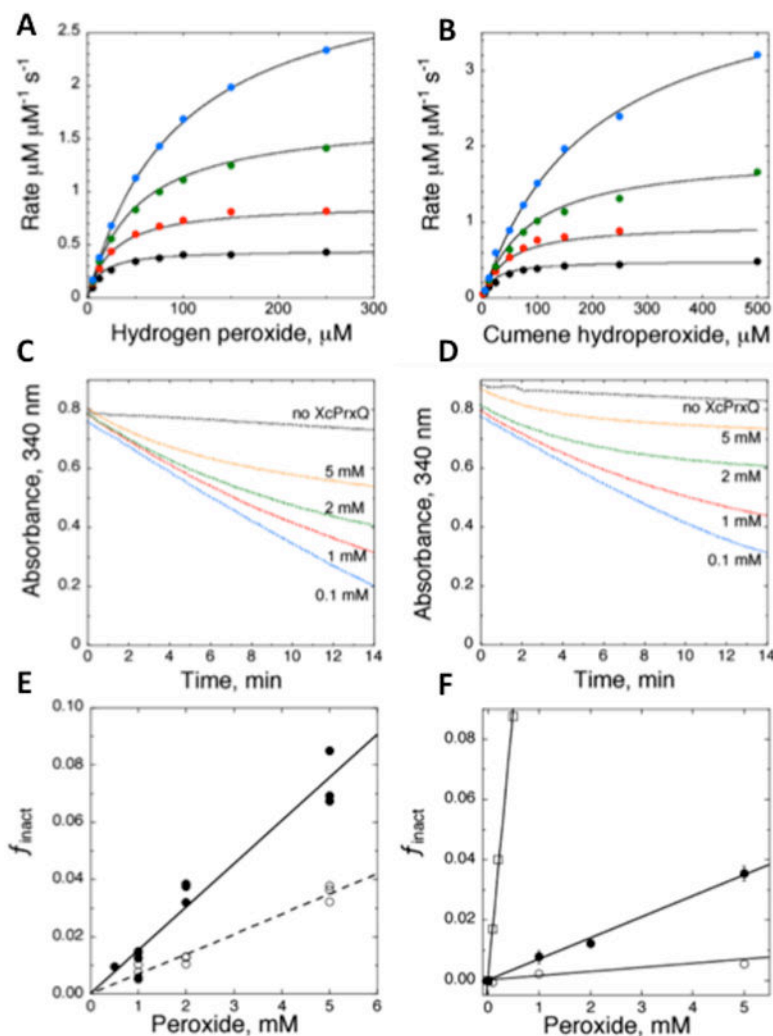


Figure 2.

In solution kinetics of *XcPrxQ*. **A.** Bisubstrate kinetics of *XcPrxQ* (0.2 μM) with hydrogen peroxide and *EcTrxA* at 5 μM (black), 10 μM (red), 20 μM (green) and 40 μM (blue). The curves are the results of the global fitting of all four data sets. **B.** Same as A, but for cumene peroxide and *EcTrxA* at 5 μM (black), 10 μM (red), 20 μM (green) and 50 μM (blue). **C–D.** Time courses showing *XcPrxQ* hyperoxidative activity loss during reactions with varying concentrations (as indicated) of hydrogen peroxide and cumene hydroperoxide, respectively. **E.** The fraction of protein inactivated per turnover (Wood et al., 2003) (f_{inact}) is plotted as a function of peroxide concentration for *XcPrxQ* hyperoxidation by hydrogen peroxide (closed circles) and cumene peroxide (open circles). **F.** Sensitivity of *XcPrxQ* to hyperoxidation by hydrogen peroxide (closed circles) is compared to literature data (Nelson et al., 2013) for human PrxI (open squares) and *Salmonella typhimurium* AhpC (open circles). See also Table S2 and Table S3.

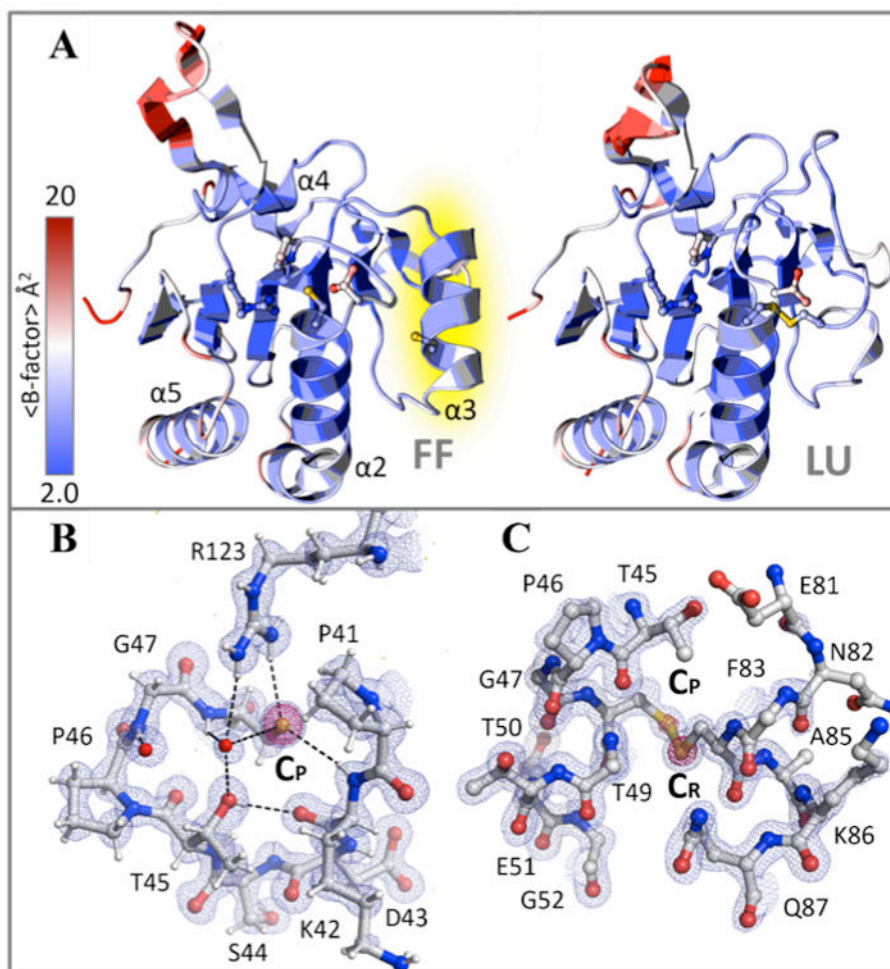


Figure 3. Fully Folded and Locally Unfolded Conformations of *XcPrxQ*. **A.** The active FF conformation (left) and the LU disulfide conformation are shown (right) as cartoons colored by local mobility as indicated by B-factor, and with sticks for C_P , C_R and the conserved active site Pro, Thr and Arg. The largest conformation changes involve the helix 3 region that is highlighted in yellow. This structural rearrangement moves C_P away from the active site pocket, disrupting all of its hydrogen bonding interactions, as described by Liao et al. (Liao et al., 2009). **B.** The active site of the *XcPrxQ* FF structure with $2F_O-F_C$ density (thin blue mesh $1.5 \rho_{rms}$ pink mesh $3.5 \rho_{rms}$). **C.** Same as B but for the LU C_P - C_R disulfide structure.

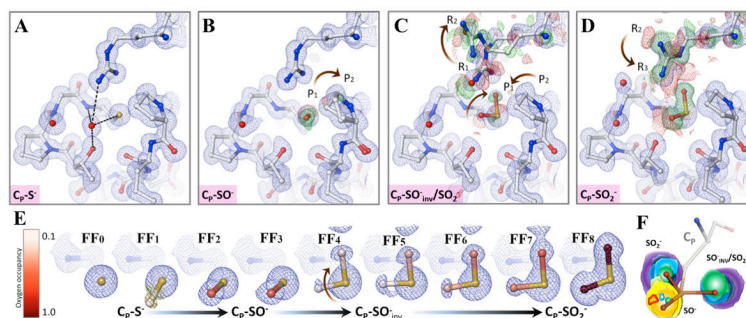
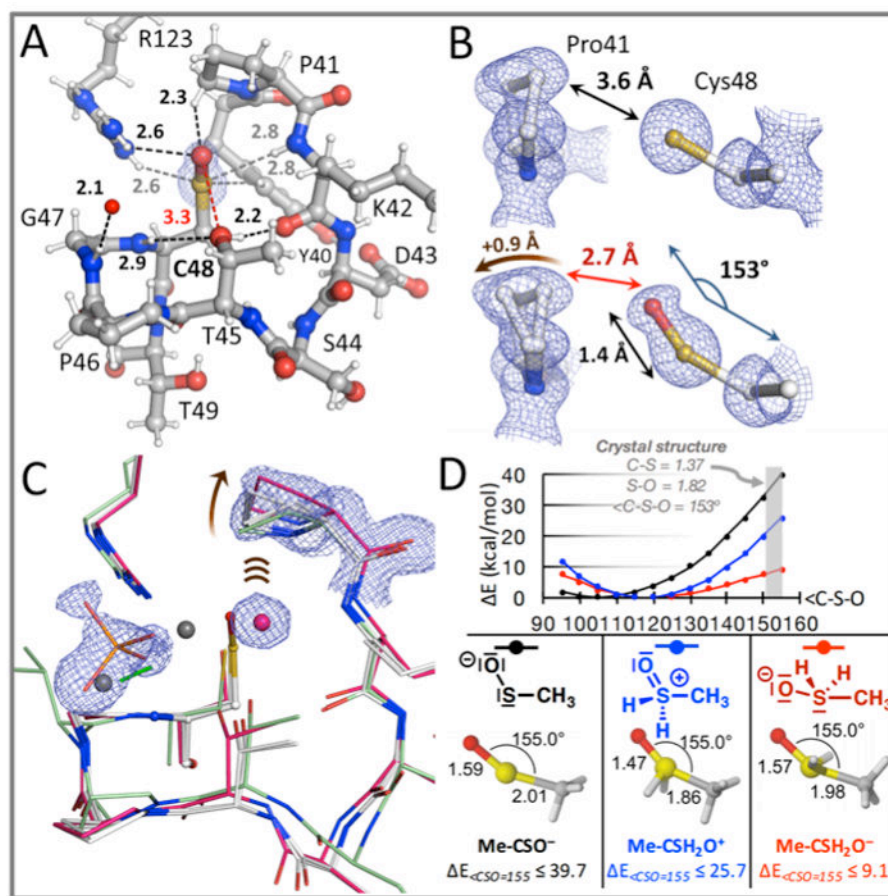


Figure 4.

Atomic resolution snapshots of XcPrxQ catalysis. **A–D.** Structures FF₀, FF₃, FF₅ and FF₈, respectively, are shown with their 2F_O-F_C electron density (blue contoured at 1.0 ρ_{rms}) and difference electron density between the structure of interest and FF₀ (green and red contoured at ±3.0 ρ_{rms}). In panels B–D, key shifts in active site residues are indicated by brown arrows with the conserved Pro flipping between two positions (noted as P1 and P2) and the Arg transitioning among three positions (R1, R2, R3). **E.** C_P is shown with occupancies of its oxygen adducts indicated by color (from light to dark red). 2F_O-F_C density is shown (blue contoured at 1.0 ρ_{rms} and for the sulfenate oxygen in FF₁ olive contoured at 0.3 ρ_{rms}). Density near the top of the image in structures FF₄-FF₇ is from a partially-occupied Arg conformation that occurs as the protein converts from the sulfenate to sulfinate state. **F.** A single image showing the 2F_O-F_C electron density peaks for C_P oxygens from all structures as single planes (solid colors at 1.0 ρ_{rms}, red outline 0.3 ρ_{rms}). The overlay shows the progression of the oxidation of C_P: from 10% SO⁻ (red outline; FF₁), 45% SO⁻ (orange; FF₂), 50% SO⁻ (yellow; FF₃), 10% SO₂⁻ (light green; FF₄), 20% SO₂⁻ (cyan; FF₅), 20% SO₂⁻ (blue; FF₆), 35% SO₂⁻ (dark blue; FF₇), 100% SO₂⁻, (purple; FF₈). All structural images were prepared using Pymol. See also Figure S3 and Figure S4.

**Figure 5.**

Unusual Cys-sulfenate geometry. **A.** Packing interactions of the Cys-sulfenate are shown for structure FF₃, highlighting interactions with the Cys-S γ (gray dashes and distances in Å), with the sulfenate oxygen (black dashes and distances), and a possibly unfavorable interaction between Thr45-OH and the C_P-SO⁻ (red dash and distance). 2F_O-F_C electron density evidence for the sulfenate position is also shown (blue contoured at 1.0 ρ_{rms}). **B.** Interaction of the C_P-thiolate with Pro41 (upper image) compared with that of the C_P-sulfenate (at 0.5 occupancy and labeled with its unusual bond angle and distance reported; lower image). A brown arrow shows the shift of Pro41-C γ accommodating the sulfenate formation by relieving a steric clash (red double-headed arrow) to increase the Pro41-C γ to sulfenate oxygen distance to 3.6 Å. **C.** Structure of C48S XcPrxQ including bound water and phosphate (pink model) is compared with the XcPrxQ thiolate (FF₀) and XcPrxQ sulfenate (FF₃) forms (similar models both with white carbons; FF₀ waters are gray spheres) and peroxide bound ApTpx (PDB code 3a2v, green carbons). Shift of the Pro is noted with a brown arrow. Notable observations are the C48S water and phosphate being near the FF₃ Cys-sulfenate oxygen and the ApTpx peroxide, respectively. **D.** Gas phase quantum mechanical calculations (Zhao and Truhlar, 2008) of methyl SO⁻, SH₂O⁺, and SH₂O⁻ species showing their energies as a function of their C-S-O bond angle (upper panel) as well as the optimized geometries and energies for the structures constrained to have a C-S-O

angle of 155°. 3D figures were generated using CYLview (Legault, 2009). See Figures S4 and S5 for supporting details.

Author Manuscript

Author Manuscript

Author Manuscript

Author Manuscript

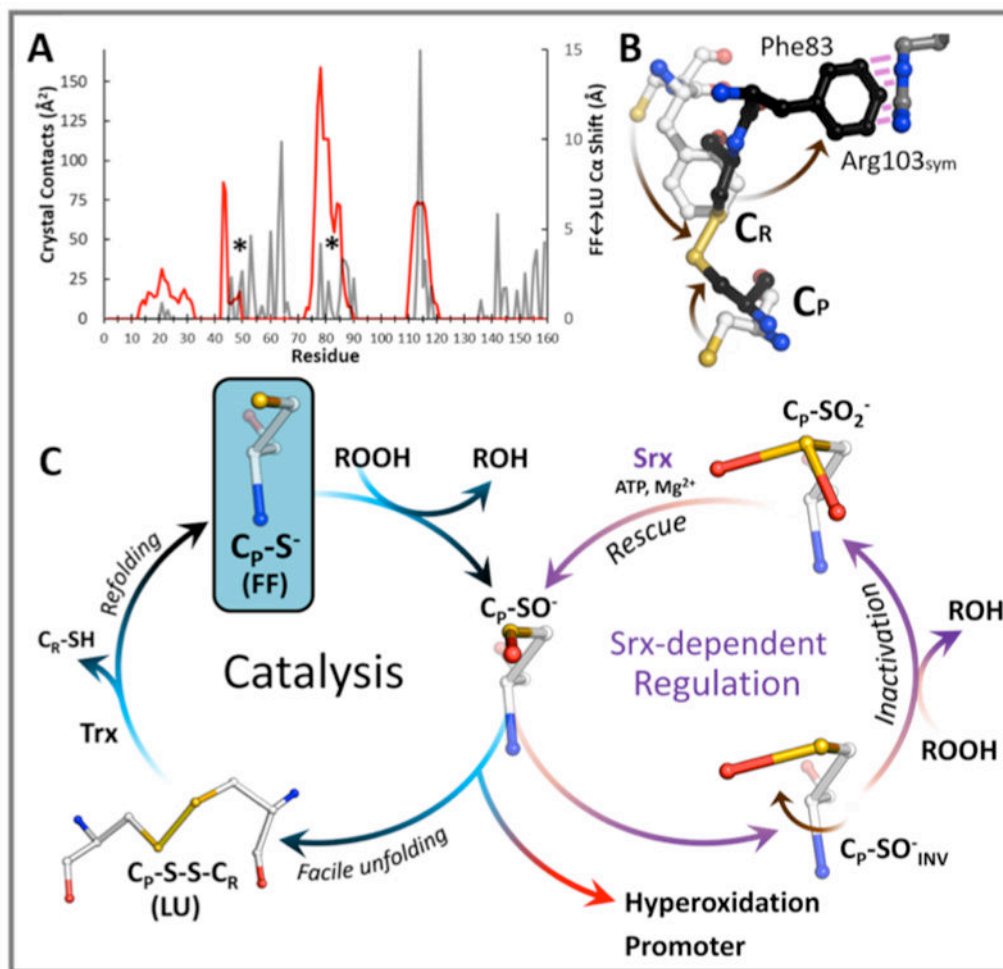


Figure 6. Non-covalent stabilization of the FF conformation can promote hyperoxidation. **A.** Protein surface area buried by crystal contacts (gray) has substantial overlap with magnitudes of conformation change (red) on a per residue basis along the chain. The C_P (Cys48) and C_R (Cys84) positions are denoted (*). Residues 79–81, not well defined in the LU structure, were assigned a shift of 10 Å based on their neighbors. **B.** One crystal contact region in the FF XcPrxQ crystals (white for main molecule and gray for symmetry mate) overlaid with LU structure (black) shows FF→LU movement (brown arrows) of Phe83 is prevented by a steric clash with Arg103 of the symmetry mate (red) because the two side chains would be 1.3 Å apart. **C.** A general mechanism for Prx catalysis and hyperoxidation is shown, as has been previously proposed (Sevilla et al., 2015)(Perkins et al., 2015)(Perkins et al., 2014), that highlights the key physiologically-relevant redox states that have been captured at atomic resolution for XcPrxQ. Also emphasized is that inhibiting facile unfolding enhances inactivation. This has been observed to occur for sensitive Prx1-subfamily members by stabilization by the C-terminal tail (Wood et al., 2003). In the case of XcPrxQ, the FF crystal form can be conceptually considered as a large non-covalent FF-conformation-stabilizing inhibitor, trapping the enzyme as FF and promoting inactivation.

Table 1

Data Collection and Refinement Statistics for Representative XcPrxQ Structures

<i>Data Collection</i>	PDB code: 5iiz	PDB code: 5ime	PDB code: 5imf	PDB code: 5iny	PDB code: 5io2
Structure	FF ₀ P2 ₁	FF ₃ P2 ₁	FF ₅ P2 ₁	FF ₈ P2 ₁	C48S P2 ₁
Space group					
Unit cell <i>a</i> , <i>b</i> , <i>c</i> (Å), γ (°)	35.4, 52.4, 40.0, 103.3	35.5, 51.2, 40.0, 104.0	35.6, 51.5, 40.0, 104.1	35.6, 51.3, 40.0, 104.0	35.6, 51.3, 39.7, 103.8
Resolution (Å)	25.5–1.05 (1.11)- γ^d	10.6–1.05 (1.11)-	23.2–1.04 (1.10)-	11.5–1.04 (1.10)-	30.8–1.20 (1.26)-
Completeness (%)	98.0 (96.7)	87.6 (50.0)	90.5 (51.0)	91.0 (51.3)	86.4 (47.6)
Unique reflections	63472 (9105)	56804 (4673)	60776 (4940)	60675 (4932)	37466 (2964)
Multiplicity	7.0 (6.9)	6.6 (4.5)	6.3 (3.8)	6.4 (3.8)	3.6 (3.0)
R _{meas} (%)	11 (14.7)	8 (9.5)	10 (13.5)	8 (12.5)	10 (7.5)
CC _{1/2}	1.0 (0.70)	1.0 (0.72)	1.0 (0.45)	1.0 (0.51)	1.0 (0.71)
$\langle I/\sigma \rangle$	11.8 (2.3)	15.8 (2.0)	11.3 (0.9)	14.3 (1.3)	8.4 (1.6)
$\langle I/\sigma \rangle \sim 2.0$ (Å) ^b	-	1.05	1.07	1.06	1.25
<i>Refinement</i>					
Resolution range (Å)	25.5–1.05	10.6–1.05	23.2–1.04	29.6–1.04	30.8–1.20
R-factor (%)	13.5	12.5	13.8	12.3	13.7
R-free (%)	15.3	14.4	16.0	14.5	16.7
Protein residues	159	158	159	159	159
Water molecules	261	308	316	311	325
RMSD lengths (Å)	0.007	0.015	0.013	0.011	0.012
RMSD angles (°)	1.0	2.0	1.8	1.7	1.3
Ramachandran plot ^c					
ϕ , ψ -Preferred (%)	100.0	100	100.0	99.4	100
ϕ , ψ -Allowed (%)	0.0	0.0	0.0	0.6	0.0
ϕ , ψ -Outliers (%)	0.0	0.0	0.0	0.0	0.0
B factors ^d					
$\langle \text{Main chain} \rangle$ (Å ²)	11	8	8	9	9
$\langle \text{Waters} \rangle$ (Å ²)	33	23	24	25	25
<i>R</i> _{pn} progression (%)	pH=7.0	pH=4.5	pH=4.5	pH=4.5	pH=5.5

<i>Data Collection</i>	PDB code: 5iiz	PDB code: 5imc	PDB code: 5imf	PDB code: 5iny	PDB code: 5io2
S ⁻	100	50	55		
SO ⁻		50	15		
SO ⁻ _{inv}			10		
SO ₂ ⁻			20	100	

^aValues in parenthesis are for the highest resolution shell and preceding values are for all data;

^bFor reference to traditional resolution cutoffs, the point where $\langle I/\sigma \rangle$ falls to ~ 2.0 is provided;

^cPreferred, allowed, and outlier angles as assigned by Molprobity (Davis et al., 2004);

^dOutliers were generally in areas of weak density, such as the C-terminal region. Please also see Table S1 for crystallographic statistics for additional structures.